

# Elucidating the Proton Source for CO<sub>2</sub> Electro-reduction on Cu(100) using Many-body Perturbation Theory

Dongfang Cheng<sup>1</sup>, Ziyang Wei<sup>2,3\*</sup>, Philippe Sautet<sup>1,2,4\*</sup>

<sup>1</sup>Department of Chemical and Biomolecular Engineering, University of California, Los Angeles, CA 90095, USA.

<sup>2</sup>Department of Chemistry and Biochemistry, University of California, Los Angeles, CA 90095, USA.

<sup>3</sup>Department of Mechanical and Aerospace Engineering, Princeton University, Princeton, NJ 08544, USA.

<sup>4</sup>California NanoSystems Institute, Los Angeles, CA 90095, USA.

\* Correspondence: [wzy@chem.ucla.edu](mailto:wzy@chem.ucla.edu), [sautet@ucla.edu](mailto:sautet@ucla.edu)

## Abstract

The protonation of CO is recognized as the rate-determining step in the generation of C1 products during the electrochemical CO<sub>2</sub> reduction reaction (CO<sub>2</sub>RR) on Cu surfaces. Despite its importance, the detailed mechanism and the precise proton source for this elementary step remain elusive and are under intense debate. Density Functional Theory (DFT) calculations have been used to investigate such a mechanism. However, semi-local functionals at the generalized gradient approximation (GGA) level face significant challenges in accurately describing adsorbate-metal interactions and surface stability. In this work, we employed the Random Phase Approximation (RPA), a method based on many-body perturbation theory, to overcome these limitations. We coupled the RPA framework with the linearized Poisson–Boltzmann equation to model solvation effects and incorporated a surface charging method to account for the influence of the electrochemical potential. Our study reveals that, in neutral or alkaline electrolytes, adsorbed water at the surface acts as the proton source for the reduction of \*CO to \*COH over a wide range of potentials via the Grotthuss mechanism. At highly negative potentials, solvent water becomes the primary proton donor, with multiple competing mechanisms observed. In contrast, DFT-GGA functionals not only significantly underestimate the reaction barriers for \*COH formation but also consistently predict solvent water as the proton source across all the potentials of interest. Additionally, RPA offers distinct insights into H<sub>2</sub>O adsorption and highlights the significant range of reducing potential within which surface \*OH can exist, which is crucial for accurate CO<sub>2</sub>RR modeling. These potential-dependent thermodynamic and kinetic data illustrate a pronounced divergence between the mechanistic insights offered by RPA and those derived from DFT-GGA functionals. Our findings offer a fresh perspective on proton transfer in CO<sub>2</sub>RR and establish a framework for future theoretical studies of electrochemical processes.

## I. Introduction

Electrochemical CO<sub>2</sub> reduction reaction (CO<sub>2</sub>RR) presents a promising strategy to close the carbon cycle<sup>1-3</sup>. Copper (Cu) is the only metal that enables the reduction of CO<sub>2</sub> into hydrocarbons such as methane, ethylene, and ethanol<sup>3-5</sup>. However, identifying the detailed mechanisms of this process remains challenging due to the short-lived nature of key intermediates, making them difficult to

be captured using experimental spectroscopy. Notably, \*CO has been identified as the main intermediate on the catalyst surface during CO<sub>2</sub>RR<sup>6-7</sup>. Both experimental and theoretical studies have demonstrated that the protonation of CO is the rate-determining step (RDS) for the generation of C1 products and plays a significant role in the formation of multi-carbon products<sup>8-10</sup>. Despite extensive research, there is still intense debate regarding the proton source and mechanism for CO protonation, many possibilities have been proposed (Table 1) and no consensus has yet been reached.

In neutral or alkaline conditions, solvent water is commonly regarded as the proton source for the proton-coupled electron transfer (PCET) process. Some groups, however, have proposed different views. Li et al. claimed that in strongly alkaline electrolytes (pH > 11), CO undergoes surface hydrogenation via adsorbed hydrogen atoms based on their measurements of Tafel slopes and reaction orders<sup>11</sup>. Chang et al. challenged the conventional view that C–C coupling is the rate-determining step (RDS) for C2 product formation. Instead, they suggested that the hydrogenation of CO with adsorbed water serves as the RDS, as supported by the analysis of the measured reaction order for CO<sup>12</sup>. Recently, Shao et al. identified surface water as the initial proton source for CO reduction on Cu at various potentials in alkaline electrolytes (pH=13) using shell-isolated nanoparticle-enhanced Raman spectroscopy (SHINERS) technology<sup>13</sup>.

Many theoretical efforts based on density functional theory (DFT) have been made to investigate this elementary step. Early studies, using the computational hydrogen electrode (CHE) model, determined that \*CHO forms on the Cu(211) surface in a thermodynamically favored manner<sup>14</sup>. Nie et al conducted the first study that explicitly considered the reaction kinetics, proposing that \*COH formation is kinetically preferred on Cu(111) via the H shuttling mechanism<sup>15</sup>. Goddard and coll. examined the reaction mechanism of CO reduction on Cu(100) at pH 7, incorporating the aqueous solvent explicitly with ab initio molecular metadynamics simulations free energy calculations<sup>16</sup>. Their findings revealed that \*CO is reduced to \*CHO via surface-bound \*H with a reaction barrier of 0.96 eV, while using solvent water as the proton source resulted in a slightly higher barrier of 0.97 eV. They further employed grand canonical DFT (GCDFT) calculations to account for the potential effects, exploring various proton sources (surface \*H, solvated H<sup>+</sup> and surface water) on Cu(111) surface<sup>17</sup>. Their results emphasized the crucial role of surface water in

determining the selectivity for hydrocarbon products over oxygen-containing alcohol products. Nørskov and coll. studied CO protonation on various Cu surfaces by establishing a monolayer of water with an additional hydronium ion, utilizing a charge extrapolation method to include potential effects. They found that \*CHO formation is preferred over \*COH<sup>8</sup>. In contrast, Bell and Head-Gordon recently argued that using hydronium ions as proton source does not represent the alkaline conditions, leading to an underestimation of the reaction barrier for PCET process<sup>18</sup>. Instead, they used explicit water and identified that at relatively positive potentials, \*CHO formation is favored, while more negative potentials promote \*COH formation.

Despite these significant advancements in understanding the proton sources and CO protonation mechanism, the aforementioned theoretical studies rely on generalized-gradient approximations (GGA) exchange correlation (XC) functionals within the DFT framework. However, these semi-local density functionals suffer from the well-known ‘CO-puzzle’ problem, failing to accurately describe the CO binding configuration and adsorption energies on Cu surfaces<sup>19-21</sup>. Given that \*CO is a critical reactant involved in CO<sub>2</sub>RR, as well as the electron self-interaction error and failure to capture the long-range electron correlation effects in DFT approximations, using these XC functionals gives rise to significant uncertainties in modeling CO<sub>2</sub>RR. Recently, several approaches beyond DFT have emerged to address these limitations. Carter et al employed embedded correlated wavefunction (ECW) theory to provide a regional correction to these XC errors. They used the Eigen cation (H<sub>9</sub>O<sub>4</sub><sup>+</sup>), which includes a hydronium ion, coupled with a charge extrapolation method to explore CO reduction. They found that the barriers for forming \*COH and \*CHO are nearly identical at relatively negative potentials, while at less negative potentials, surface \*H is preferred as the proton source<sup>22-23</sup>. The Random Phase Approximation (RPA), another post-Hartree Fock(HF) method based on many-body perturbation theory, offers a promising alternative for tackling such surface catalysis problems<sup>19-20, 24-25</sup>. The RPA method circumvents the symmetry mismatch between the embedded cluster and the metallic surface encountered in ECW approach, benefitting from its implementation with plane waves in periodic boundary conditions. Our recent work employed RPA to investigate the mechanisms of CO<sub>2</sub>RR and identified that \*CHO formation is thermodynamically more favorable<sup>26</sup>.

In this study, we employed the RPA combined with the linearized Poisson–Boltzmann (IPB) equation to account for solvent effects and integrated a surface charging method within the GCDFT framework to incorporate the influence of the electrochemical potential. This approach allowed us to investigate the detailed mechanism and proton source for CO reduction by proton-coupled electron transfer on the Cu(100) surface in neutral or alkaline electrolytes. Our findings revealed that water adsorbed on the surface acts as the proton source for the protonation of \*CO to \*COH across a wide range of potentials, through the Grotthuss mechanism. At highly negative potentials, solvent water becomes the dominant proton source, with multiple competing mechanisms emerging under these conditions. In contrast, DFT-GGA functionals consistently predict that solvent water serves as the proton donor across all the relevant potentials. Moreover, they inadequately describe the adsorption of water and hydroxyl, both of which are crucial in modeling CO<sub>2</sub>RR. These potential-dependent energetic discrepancies highlight a significant divergence between the mechanistic insights provided by RPA and those obtained from DFT-GGA functionals, underscoring the limitations of the latter in accurately modeling CO<sub>2</sub>RR on Cu surfaces.

**Table 1.** Summary of proposed reaction mechanism of CO reduction via different proton sources.

Mechanism	Proton source	Elementary steps
M1	H <sub>2</sub> O(l)	*CO + H <sub>2</sub> O + e <sup>-</sup> → *COH + OH <sup>-</sup> or *CO + H <sub>2</sub> O + e <sup>-</sup> → *CHO + OH <sup>-</sup>
M2	surface *H	H <sub>2</sub> O + e <sup>-</sup> → *H + OH <sup>-</sup> and *CO + *H → *CHO
M3-1	via isolated *H <sub>2</sub> O	*CO + *H <sub>2</sub> O + e <sup>-</sup> → *CHO + OH <sup>-</sup> or *CO + *H <sub>2</sub> O → *CHO + *OH
M3-2	surface *H <sub>2</sub> O via Grotthuss mechanism	*CO + *H <sub>2</sub> O-H <sub>2</sub> O + e <sup>-</sup> → *CHO + OH <sup>-</sup> or *CO + *H <sub>2</sub> O-H <sub>2</sub> O → *CHO + *OH or *CO + *H <sub>2</sub> O-H <sub>2</sub> O + e <sup>-</sup> → *COH + OH <sup>-</sup> or *CO + *H <sub>2</sub> O-H <sub>2</sub> O → *CHO + *OH

## II. Results and Discussion

**Thermodynamic scheme.** Figure 1 illustrates the RPA energetics of CO reduction intermediates across different mechanisms, in comparison with GGA-level PBE and RPBE energetics on a Cu(100) surface. This thermodynamic analysis is based on the energetics calculated at the potential

of zero charge (PZC) and does not specifically account for potential effect. The adsorption free energies are referenced to the bare surface and gas phase of the molecules. In Mechanism 1 (M1), it is evident that the PBE functional strongly overbinds CO, while the RPBE functional exhibits binding energies similar to RPA. However, neither PBE nor RPBE accurately predicts the atop-site binding of CO. For the intermediates \*COH and \*CHO, PBE shows an overbinding of approximately 0.5 eV and 0.1 eV, respectively. Conversely, RPBE underestimates the binding energy for both, and predicts a thermodynamic similarity in forming \*CHO and \*COH, whereas PBE and RPA indicate a preference for \*COH or \*CHO formation, respectively. In Mechanism 2 (M2) involving \*H adsorption, PBE slightly overbinds, while RPBE does the opposite.

In Mechanism 3 (M3), where surface water is involved in the protonation process, the adsorption of water is critical. Weak adsorption of H<sub>2</sub>O prevents its involvement in surface reactions. As shown in Figure 1c, PBE and RPA display a slightly negative adsorption free energy for one \*H<sub>2</sub>O, whereas RPBE underestimates this adsorption by about 0.2 eV. At neutral conditions, PBE and RPA find that hydroxyl (\*OH) is more stable on the surface, compared to OH<sup>-</sup> in the solution. In contrast, RPBE indicates a weak \*OH adsorption, leading to the more favorable formation of OH<sup>-</sup> in the solution at PZC.

Besides isolated surface \*H<sub>2</sub>O acting as a proton source, proton transfer can also occur via the Grotthuss mechanism (M3-2). In this mechanism, one water molecule adsorbs on the surface, and another water molecule connects to it via hydrogen bonding, denoted as \*H<sub>2</sub>O-H<sub>2</sub>O. The other H of the latter serves as the proton donor. During the PCET process, one H from the adsorbed H<sub>2</sub>O transfers to the adjacent H<sub>2</sub>O concurrently, leaving \*OH on the surface or forming OH<sup>-</sup> (denoted as \*OH-H<sub>2</sub>O and [H<sub>2</sub>O-OH<sup>-</sup>], respectively), which is known as the ‘H-shuttling’ mechanism. Co-adsorption of \*CO and \*H<sub>2</sub>O-H<sub>2</sub>O is highly favorable with PBE due to the overbinding of both \*CO and \*H<sub>2</sub>O, while it is slightly unfavorable with RPA. Similar to the isolated H<sub>2</sub>O case, RPBE shows strongly unfavorable \*OH binding, resulting in high energy levels for \*COH + \*OH-H<sub>2</sub>O and \*CHO + \*OH-H<sub>2</sub>O. In both scenarios, the formation of \*COH is more favorable with PBE and, in contrast, RPA predicts that forming \*CHO is preferred thermodynamically at PZC.

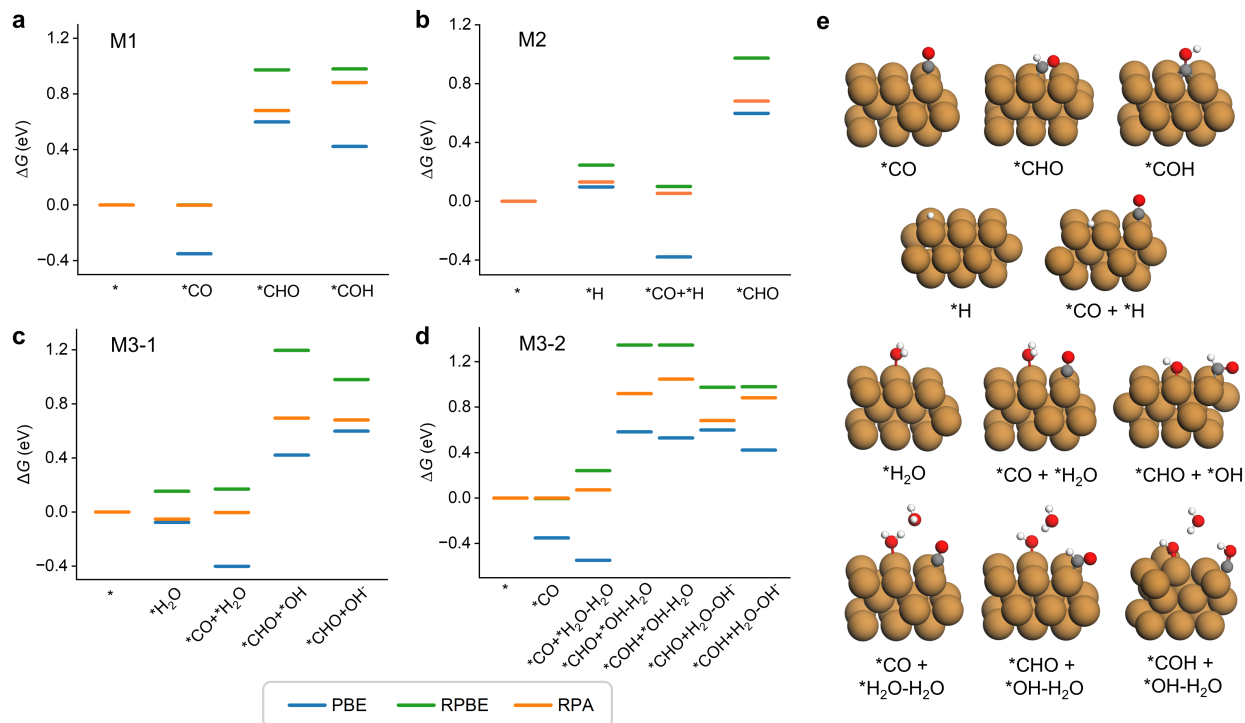


**Figure 1.** Energetics of CO reduction intermediates involved in various mechanisms (a) M1 (from solvent H<sub>2</sub>O) (b) M2 (from surface \*H) (c) M3-1 (from isolated adsorbed \*H<sub>2</sub>O) and (d) M3-2 (from adsorbed \*H<sub>2</sub>O via Grotthuss mechanism) using RPA and PBE/RPBE functionals on the Cu(100) surface; (e) Atomic structures of key intermediates involved in the four mechanisms. For adsorbates with multiple possible sites, we consider the one with the most stable RPA energy. Cu atoms are shown as brown, O atoms red, C atoms grey, and H atoms white.

**Solvent water serves as the proton source.** In the following sections, we will model the pH and potential-dependent thermodynamics and kinetics for each mechanism to uncover the full picture beyond the thermodynamics scheme at the PZC. To simulate the electrochemical interface, we adopted a hybrid solvent model comprising an explicit water cluster with an implicit solvent model. The former serves as the proton donor and represents the short-range solvation and the latter accounts for the long-range solvation effects. We used a surface charging method within the GCDFT framework to incorporate the potential effect. For details, see method.

The first scenario involves solvent water as the proton source, a widely accepted mechanism. At PZC conditions, RPBE shows competitive behavior between forming \*CHO and \*COH. However, when the potential effect is included (in the range [-2;0] V vs SHE), \*CHO formation becomes

consistently more thermodynamically favorable. RPA also shows a strong preference for \*CHO formation across the potential of interest. In contrast, the PBE functional indicates that at less negative potentials, \*COH formation is preferred, consistent with predictions at PZC. As the potential becomes more negative, there is a switch favoring \*CHO formation. Additionally, the thermodynamic onset potentials for PBE and RPBE (corresponding to  $\Delta\Omega = 0$ ) are similar, both around -1.35 V vs SHE at pH = 7, shifting to more negative values as the pH increases (by  $k_B \cdot T \cdot \Delta\text{pH}$ ), while RPA predicts a slightly more positive onset potential (-1.25 V vs SHE)

We then mapped the minimum energy paths for proton transfer leading to the formation of \*CHO and \*COH. For RPA, CO initially adsorbs at the top site. One H<sub>2</sub>O molecule within the cluster gradually approaches the adsorbed \*CO and donates one proton to either C or O, forming \*CHO and \*COH, respectively. Concurrently, another adjacent H<sub>2</sub>O molecule in the cluster transfers a proton to the donating H<sub>2</sub>O molecule, establishing a systematic hydrogen-bonding network. In the transition state for \*H-CO, the \*CO remains at the top site, whereas for \*CO-H, the \*CO diffuses to the hollow site. In the final state, \*CHO binds via a bidentate atop adsorption, while \*COH resides in the hollow site, with two water molecules stabilizing the resulting OH<sup>-</sup> through hydrogen bonding. For PBE and RPBE, \*CO initially adsorbs at hollow and bridge sites, with the \*H-CO and \*CO-H transition states located on bridge and hollow sites, respectively.

Despite thermodynamic predictions favoring \*CHO formation under negative potentials, kinetic modeling reveals significantly lower barriers for \*COH formation with PBE and RPBE. The charge transfer coefficient is more pronounced with PBE, leading to a sharper decrease in reaction barriers with more negative potential compared to RPBE, resulting in an almost barrierless formation of \*COH at -2 V vs SHE. At pH = 14, the reaction energy is higher than the reaction barriers, particularly for forming \*COH, as the reaction energy of PCET steps shifts with pH changes, while the reaction barrier remains unchanged on the SHE scale. In this case, we assume no additional barrier, and the reaction energy can be considered the reaction barrier, consistent with observation in Carter's work<sup>22</sup>.

In contrast, the potential-dependent reaction barrier behavior with RPA is notably different. The barrier for forming \*CHO is similar to that using GGA functionals, however, the barrier for

forming \*COH is significantly higher. The charge transfer coefficient for forming \*COH is slightly larger than that for forming \*CHO, leading to a crossover point where the \*CHO pathway is kinetically more favorable at less negative potentials and vice versa. The energy difference between these two pathways is however minimal, making the formation of \*CHO and \*COH highly competitive across the entire potential range. Even at highly negative potentials, the reaction barriers using RPA are still high, reaching about 1 eV. This stark difference indicates that PBE and RPBE significantly overestimate the binding energy of the transition state \*CO-H. The transition state, adsorbed in the hollow site, involves a proton from the water cluster connecting with the oxygen atom of \*CO through hydrogen bonding. Consequently, the electronic state of Cu-\*CO-H remains unchanged from that of pure CO adsorbed on the surface. Therefore, the well-known ‘CO puzzle’ problem persists in describing the transition state of \*CO-H. PBE and RPBE overestimate the adsorption energy of hollow site \*CO, resulting in underestimated reaction barriers for \*COH formation.

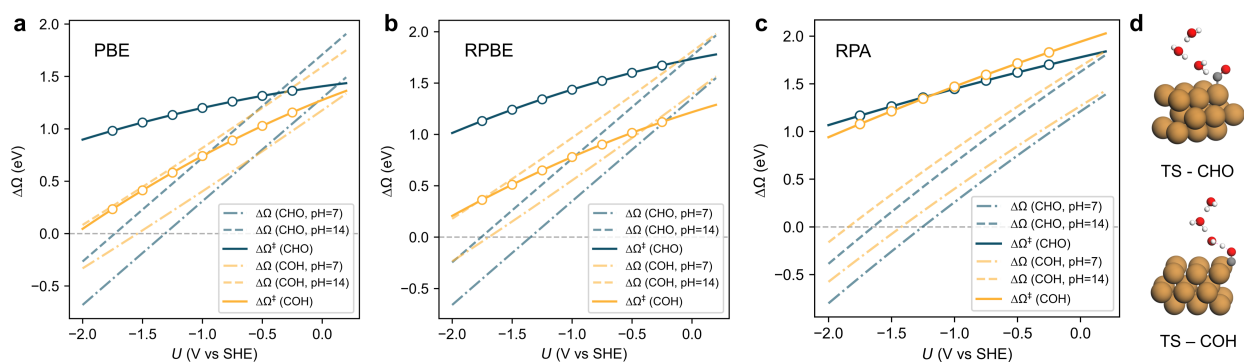


**Figure 2. Solvent water as the proton source in CO protonation (M1).** Potential-dependent grand canonical reaction free energy ( $\Delta\Omega$ ) (dashed lines) and reaction barrier ( $\Delta\Omega^\ddagger$ ) (solid lines) of CO protonation to \*CHO (dark blue) and \*COH (orange) on Cu(100) using (a) PBE (b) RPBE functionals and (c) RPA. (d) The transition state of forming \*CHO and \*COH.

**Surface \*H acts as the proton source.** Surface \*H is often considered the proton source for protonation of \*CO. This hypothesis is reasonable to some extent, as H is predicted to be the dominant adsorbate via thermodynamic sampling at negative potentials, providing an opportunity for surface \*H to act as the proton source<sup>27-28</sup>. We found that the potential-dependent behaviors of \*H adsorption are consistent when using PBE, RPBE, and RPA. In both PBE and RPA, \*H does

not adsorb onto the surface until -0.95 V vs SHE, while RPBE slightly underbinds it, delaying adsorption by about 0.1 V. The slopes of these adsorption behaviors are close to 1, as H adsorption energy is linearly correlated with the electrode potential (Figure 3a, dashed lines).

Surface \*H originates from the solvent via the Volmer step, a crucial elementary step in the hydrogen evolution reaction (HER). As depicted in Figure 3a, PBE shows the lowest reaction barrier for the Volmer step, followed by RPBE and RPA. PBE underestimates the Volmer barrier by about 0.5 eV across the potential range. Nevertheless, the barriers obtained here are significantly higher than those using hydronium ion as the proton source<sup>18, 22, 28-29</sup>, indicating that under neutral or alkaline conditions, despite the thermodynamic prediction of high \*H coverage at negative potentials, the process would still be kinetically limited.

We then examined the \*H coupling with \*CO to form \*CHO. Under neutral conditions, the reaction free energies are 0.97 eV, 0.87 eV, and 0.62 eV for PBE, RPBE, and RPA, respectively. When the potential effect is considered, all reaction energies decrease. Although surface hydrogenation is a chemical step rather than an electrochemical step, the reaction energy still exhibits potential dependence, showing significant parabolic characteristics. This indicates that surface capacitance changes markedly before and after the reaction. Regarding reaction barriers, both PBE and RPBE functionals consistently underestimate them across a wide range of potentials, with charge transfer coefficients of 0.08 eV/V and 0.04 eV/V, respectively. This suggests that the barriers are not highly sensitive to the electrode potential. Conversely, RPA shows a much higher charge transfer coefficient of 0.28 eV/V. This significant potential dependence observed with RPA is due to differences in the adsorption sites: in PBE and RPBE calculations, both the initial state \*CO and transition state \*H-CO adsorb at bridge or hollow sites, while in RPA calculations, \*CO initially adsorbs at the atop site and diffuses to the bridge site in the transition state. This change in binding sites significantly alters the capacitance and PZC before and after the reaction, thus exhibiting strong potential-dependence nature with RPA.

Combining the Volmer step with the surface hydrogenation step, it is evident that both steps are potential-dependent, with the former being significantly more so. Across nearly all potentials, PBE and RPBE underestimate the barriers for both steps. Within the potential range of interest (< -1 V

vs SHE), for PBE, surface hydrogenation primarily limits the overall reaction, whereas the Volmer step is the rate-determining step for both RPBE and RPA.

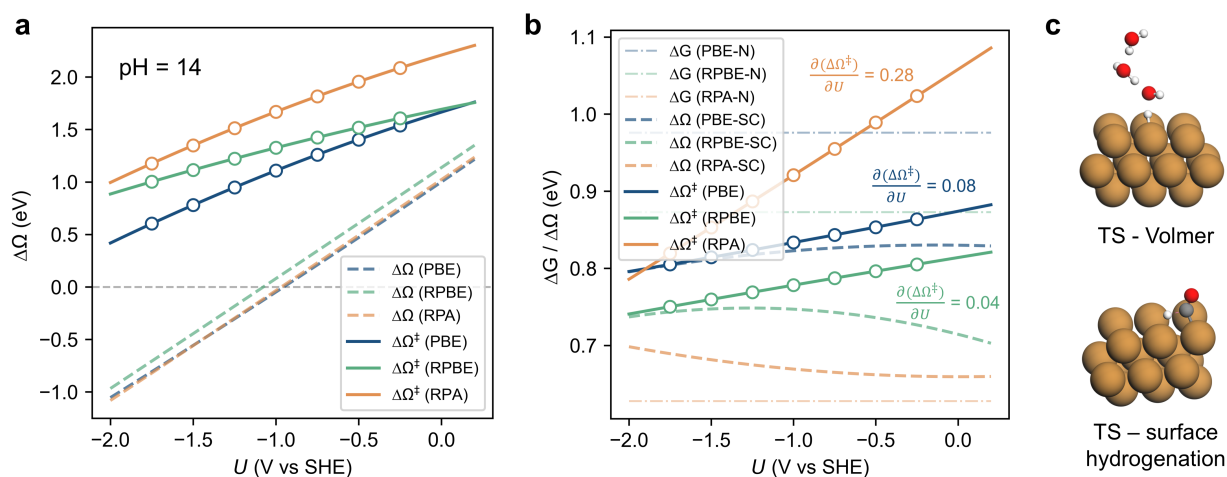


**Figure 3. Surface \*H generated by Volmer step as the proton source (M2).** Potential-dependent grand canonical reaction free energy ( $\Delta\Omega$ ) (dashed lines) and reaction barrier ( $\Delta\Omega^\ddagger$ ) (solid lines) of (a) Volmer step to form an \*H on the surface from solvent water (b) hydrogenation of \*CO via surface \*H to \*CHO using PBE (dark blue), RPBE (green) functionals and RPA (orange). In figure 3b, N represents the neutral condition, and no potential effect is included while SC represents the surface charging method, which introduces the potential effect into the energetics. The transition state for (c) the Volmer step and (d) the surface hydrogenation step.

**Isolated \*H<sub>2</sub>O as the proton source.** Surface-adsorbed \*H<sub>2</sub>O has been considered as a potential proton source in CO<sub>2</sub>RR, alongside the solvent water and surface \*H. It is crucial first to determine whether H<sub>2</sub>O can adsorb on the surface under reactive conditions. Figure 4a shows that at neutral potential (0 V vs SHE), RPBE predicts a positive adsorption free energy of 0.15 eV, while PBE and RPA show slightly negative values, indicating weak adsorption. The adsorption free energy exhibits strong potential dependence, decreasing sharply as the potential becomes more negative, with less negative potentials favoring \*H<sub>2</sub>O adsorption. Additionally, even at 0 V vs SHE, RPBE suggests that H<sub>2</sub>O adsorption remains unfavorable. The crossovers for favorable adsorption occur at -0.63 V vs SHE and -0.72 V vs SHE for PBE and RPA, respectively. Nonetheless, \*H<sub>2</sub>O adsorption is still unfavorable at reactive potentials (< -1 V vs SHE). This strong potential dependence aligns with experimental and theoretical findings, where the orientation of interfacial H<sub>2</sub>O shifts from O-down to H-down as the potential becomes more negative<sup>30-31</sup>. This occurs

because water is a polar molecule, with oxygen carrying a partial negative charge and hydrogen a partial positive charge. When an external electric field is applied, the dipole moment of the water molecules aligns with the field. At more negative potentials, water molecules reorient to position the negatively charged oxygen atoms away from the negatively charged surface, minimizing repulsive interactions.

Next, we examined the protonation process. When surface  $^*H_2O$  donates a proton to  $^*CO$ , it either leaves  $^*OH$  on the surface (a chemical reaction) or forms  $OH^-$  in the solution (an electrochemical reaction). The formation of  $OH^-$  is highly potential and pH-dependent, while  $^*OH$  formation is less sensitive to the electrode potential, as illustrated in Figure 4b. The difference between PBE, RPBE, and RPA is significant. RPBE predicts the crossover at  $-0.16$  V vs SHE, followed by PBE at  $-0.43$  V vs SHE, and RPA at  $-1.15$  V vs SHE under neutral electrolyte conditions (pH=7). This suggests that  $^*OH$  cannot be stabilized on the surface using GGA functionals, while RPA predicts a much broader potential range for  $^*OH$  stability. Experimental spectroscopic evidence, such as Raman, shows that  $^*OH$  can be present at very negative potentials ( $< -1$  V vs SHE), and its coexistence with  $^*CO$  significantly impacts surface restructuring and reaction pathways<sup>13, 32-34</sup>. However, RPBE fails to capture this behavior, underlining the limitations of using RPBE for  $CO_2RR$  studies, where it is commonly used due to its similar  $^*CO$  binding energy to RPA. The mismatch between RPBE predictions and experimental observations warrants further investigation.

Regarding the reaction barriers for forming  $^*CHO$ , PBE and RPBE significantly overestimate these barriers compared to RPA. However, RPA still predicts a high barrier for protonation from surface  $^*H_2O$ , particularly when compared to solvent water or surface  $^*H$  as proton donors. Given the unfavorable adsorption of  $^*H_2O$  under reducing conditions, it can be concluded that isolated surface  $^*H_2O$  is unlikely to be the proton source in  $CO_2RR$ .

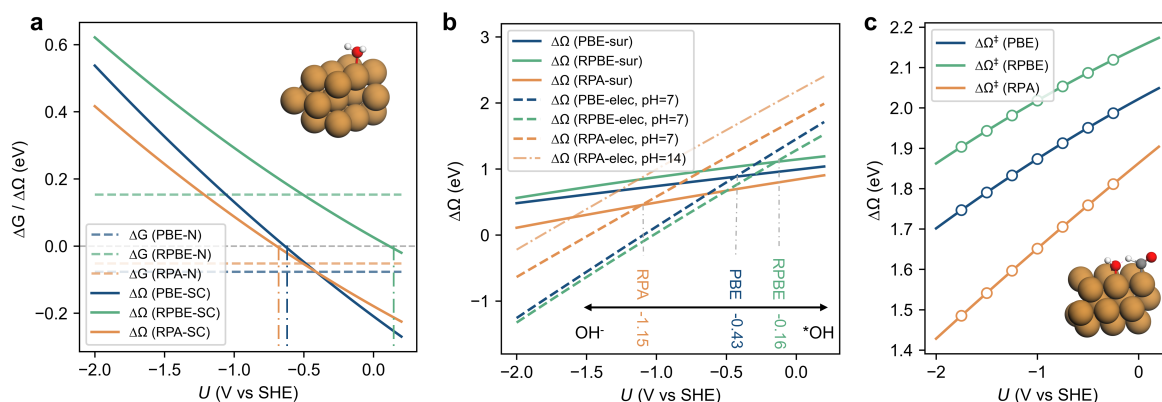


**Figure 4. Adsorbed H<sub>2</sub>O molecule as the proton source (M3-1).** (a) Adsorption of \*H<sub>2</sub>O in the neutral condition ( $\Delta G$ ) (dashed line) and charged condition ( $\Delta\Omega$ ) using the surface charging method (solid line). (b) Potential-dependent grand canonical reaction free energy ( $\Delta\Omega$ ) of CO protonation to \*CHO via surface H<sub>2</sub>O. In the final state, either adsorbed \*OH on the surface (denoted as \*-sur) or OH<sup>-</sup> in the solution (denoted as \*-elec) will be formed, the former is considered as a chemical reaction while the latter is regarded as an electrochemical reaction. The crossovers of forming \*OH or OH<sup>-</sup> are -0.16 V (RPBE), -0.43 V (PBE), and -1.15 V (RPA) in the neutral pH condition (pH = 7), all in the SHE scale. (c) Potential-dependent grand canonical reaction barrier ( $\Delta\Omega^\ddagger$ ) for CO protonation using PBE/RPBE functionals and RPA. The atomic structure of the transition state is inserted into the figure.

**Surface water as the proton source via Grotthuss mechanism.** The high barrier observed via isolated \*H<sub>2</sub>O is likely due to the relatively strong O-H covalent bond, making it less effective in donating protons to \*CO. The Grotthuss mechanism, which involves rapid proton transfer through a network of hydrogen bonds, mitigates this limitation by lowering the energy barriers associated with proton transfer. This mechanism has been demonstrated in various proton transfer processes<sup>35-38</sup>, as it allows protons to move efficiently without requiring substantial rearrangements of the surrounding molecular structure. Motivated by this, in this section, we consider the Grotthuss mechanism for the surface proton transfer process.

We consider a model involving two interconnected water molecules: one adsorbed on the surface and the other connected via hydrogen bonding. Figure 5a illustrates the potential-dependent adsorption energy of the initial state, the co-adsorption of \*CO and \*H<sub>2</sub>O-H<sub>2</sub>O. As expected, the RPBE functional fails to stabilize this initial state even at weakly negative potentials, primarily due to its underestimation of \*H<sub>2</sub>O binding. In contrast, the PBE functional shows negative

adsorption energy across the entire potential range, attributed to its overestimation of \*CO binding. The RPA functional provides a more balanced perspective, indicating that this initial state can be stabilized at relatively less negative potentials, while more negative potentials disfavor adsorption due to the strong repelling effect of adsorbed water.

Given the unfavorable adsorption of the initial state under certain potentials, it is crucial to consider the adsorption energy of the molecules when evaluating reaction kinetics, as depicted in Figure 5b. The effective barrier ( $\Delta\Omega_{\text{eff}}^\ddagger$ ), which combines the reaction barrier ( $\Delta\Omega^\ddagger$ ) and adsorption energy ( $\Delta\Omega_{\text{ads}}$ ), is the appropriate metric for assessing reaction kinetics. Moreover, in electrochemical reactions, the final state—where hydroxide is within the inner double layer—does not fully represent a solvated bulk hydroxide, necessitating a correction in the energy difference between these states, which has been in detail discussed in previous works<sup>39-40</sup>.

Next, we analyze the thermodynamics and kinetics of the protonation process via the Grotthuss mechanism. For the protonation of \*CO to \*CHO and \*COH (Figure 5c and d), similar to the case with isolated \*H<sub>2</sub>O, we observe that negative potentials favor the electrochemical reaction, leading to the formation of OH<sup>-</sup> ions rather than \*OH on the surface. However, RPA calculations suggest that \*OH can remain on the surface at more negative potentials compared to what PBE and RPBE predict. In terms of kinetics, both PBE and RPBE underestimate the barriers to form \*CHO and overestimate the barriers to form \*COH. It should be noted that no additional barriers were observed when H<sub>2</sub>O donates a proton to \*CO to form \*COH, thus the reaction energy was used as a proxy for the reaction barrier, consistent with that in the previous section. Notably, RPA shows a significant reduction in the barrier for forming \*COH via the Grotthuss mechanism compared to that via isolated \*H<sub>2</sub>O as the proton source. However, it is crucial to keep in mind that the effective barrier, rather than the reaction barrier, is essential for accurately assessing reaction kinetics.

Figure 5e summarizes the effective barriers: for the PBE functional, where \*CO and \*H<sub>2</sub>O-H<sub>2</sub>O adsorption is always favorable, the effective barriers are equivalent to the reaction barriers. Conversely, RPBE shows the opposite. For RPA, when the potential is more negative than -0.42 V vs. SHE (indicated by the dashed horizontal line), the positive adsorption energy must be included in the effective barrier, leading to an inflection point in the barrier-potential relationship.

At potentials more positive than this inflection point, the barrier decreases as the potential becomes more negative; however, beyond this point, strong unfavorable initial state adsorption reverses the trend. Notably, forming \*COH is consistently more favorable than \*CHO across PBE, RPBE, and RPA in kinetics.

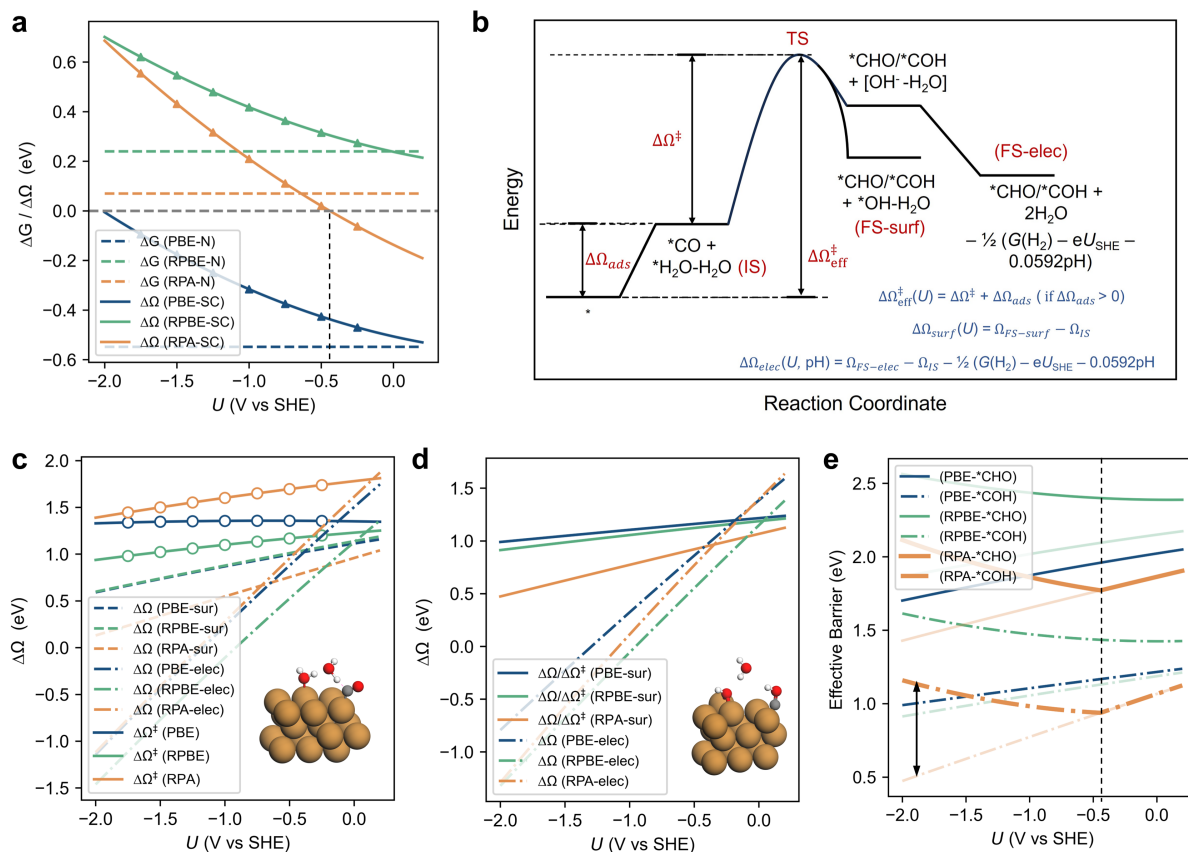


**Figure 5. Adsorbed H<sub>2</sub>O molecule as the proton source via the Grotthuss mechanism (M3-2).** (a) Adsorption of \*CO and \*H<sub>2</sub>O-H<sub>2</sub>O in the neutral condition ( $\Delta G$ ) (dashed line) and charged condition ( $\Delta \Omega$ ) using the surface charging method (solid line). (b) Schematic of the reaction energy landscape of CO protonation process via the Grotthuss mechanism. Potential-dependent grand canonical reaction free energy ( $\Delta \Omega$ ) and reaction barriers ( $\Delta \Omega^\ddagger$ ) for CO protonation to (c) \*CHO and (d) \*COH. In the final state, the formation of the adsorbed \*OH-H<sub>2</sub>O on the surface is denoted as \*-sur, and the formation of [H<sub>2</sub>O-OH<sup>-</sup>] in the solution is denoted as \*-elec, the former is considered as an chemical reaction while the latter is regarded as an electrochemical reaction. It should be noted that the reaction pathway for forming \*COH is always uphill, and no additional barrier is found in searching for the transition state, thus for \*COH formation, the reaction barrier is considered as the reaction energy. The atomic structure of the transition state (\*CHO) and final state (\*COH) are inserted in (c) and (d) respectively. (e) Effective potential dependent reaction

barriers for CO protonation to form \*CHO and \*COH using RBE/RPBE functionals and RPA, the vertical dashed line indicating the point where the adsorption of \*CO and \*H<sub>2</sub>O-H<sub>2</sub>O is thermodynamically unfavorable ( $\Delta\Omega > 0$ ) using RPA.

**Comparison of different mechanisms.** Up to this point, we have analyzed the thermodynamics and kinetics of various mechanisms using DFT-level functionals (PBE, RPBE) and RPA calculations, and by incorporating the surface charging method, we obtained comprehensive potential-dependent energetics. In this section, we systematically compare these mechanisms across different computational methods, with a particular focus on identifying the proton source. All energetics reported in Figure 6 are effective barriers.

For the PBE functional (Figure 6a), using isolated \*H<sub>2</sub>O as the proton source results in the highest reaction barrier across the potential range, eliminating it as a viable candidate. Only near 0 V vs SHE does surface water via the Grotthuss mechanism emerge as the most favorable proton source. As the potential becomes negative, solvent water becomes the preferred proton source for forming \*COH. Notably, there is a sharp decrease in the reaction barrier with increasingly negative potentials; at -2 V vs SHE, the barrier is nearly nonexistent. This low barrier would suggest an extremely high reaction rate under negative potentials, reaching up to 10<sup>7</sup> 1/s at -1.5 V vs SHE (~0.4 eV barrier) and 10<sup>12</sup> 1/s at -2 V vs SHE (~0.1 eV barrier) based on Arrhenius analysis. Given that PBE significantly overestimates \*CO binding energy, the reaction kinetics are unlikely to be limited by \*CO coverage. The situation is similar with RPBE, where the underestimation of both \*OH binding and reaction barriers for forming \*COH via solvent water shifts the crossover ([M3-2]-COH and [M1]-COH) to less negative potentials. Moreover, the other protonation pathways are less competitive within the relevant potential range.

RPA calculations reveal a different scenario. Over a wide potential range (0 V to -1.72 V vs SHE), surface water is the predominant proton source, with \*CO protonating to \*COH via the Grotthuss mechanism. The barrier does not decrease monotonically with more negative potentials due to the unfavorable adsorption of \*H<sub>2</sub>O at negative potentials. At moderately negative potentials (until -1.5 V vs SHE), other mechanisms are less competitive due to much larger reaction barriers observed compared to that of [M3-2]. However, when the potential drops below -1.72 V vs SHE, solvent water becomes the proton source for protonating \*CO to \*COH. At these negative

potentials, several mechanisms, such as surface \*H as the proton source (green line) and \*CO to \*CHO via solvent water (blue line), become competitive. We hypothesize that at very negative potentials, \*CO to \*COH via solvent water dominates, although other mechanisms may also contribute. Due to the unfavorable adsorption of \*H<sub>2</sub>O at relatively negative potentials, surface \*H<sub>2</sub>O coverage may be limited, potentially shifting the crossover of [M3-2]-COH and [M1]-COH to less negative potentials. Nevertheless, at the onset potential for methane production in CO<sub>2</sub>RR<sup>41</sup> (~-1.2 V vs SHE), surface water is likely to be the initial proton source.

The high reaction barriers (~1 eV) observed even at markedly negative potentials in RPA calculations indicate low reaction rates for C1 product formation on the Cu(100) surface. This aligns with experimental evidence showing extremely low CO<sub>2</sub>RR activity on ultraclean UHV-prepared Cu(111) and Cu(100) single crystal surfaces<sup>42</sup>. Our recent work suggests that planar Cu surfaces restructure to stepped or kinked surfaces under reaction conditions. These under-coordinated sites could potentially enhance \*H<sub>2</sub>O adsorption and then lower the effective barriers via the Grotthuss mechanism<sup>43</sup>. Additionally, Chan et al. found that the tilt of \*CO is more facile on stepped sites, facilitating its acceptance of protons<sup>8</sup>. Therefore, we hypothesize that modeling on stepped or kinked surfaces using RPA would yield results more consistent with experimental data on polycrystalline Cu<sup>41</sup>. Nevertheless, our findings on Cu(100) provide valuable insights and reveal the fundamental mechanism underlying CO protonation.

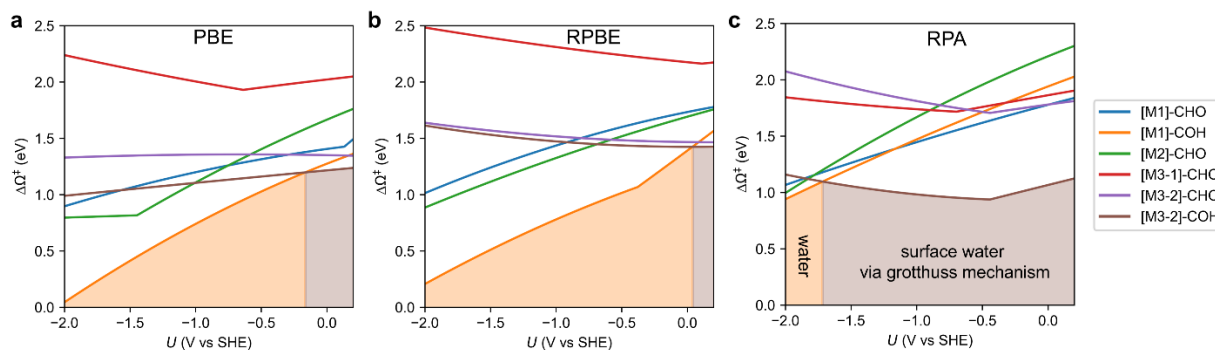


**Figure 6.** Comparison of (a) PBE, (b) RPBE functional, and (c) RPA in predicting the proton source and the reaction barrier of CO protonation. The colored shadowed region represents the dominant region for a specific mechanism.

### III. Conclusions

To summarize, we employed RPA, combined with the linearized Poisson–Boltzmann equation and the surface charging method, to investigate the mechanism of CO reduction in CO<sub>2</sub>RR on the Cu(100) surface. Our results reveal a substantial difference between RPA and DFT-GGA functionals. In alignment with the experimental spectroscopic findings, RPA calculations demonstrated that surface water acts as the initial proton source via the Grotthuss mechanism across a wide range of potentials, reducing \*CO to \*COH. Only under highly negative potential does solvent water become the dominant proton source. In contrast, GGA-level functionals strongly underestimate the reaction barriers for \*COH formation and predict that the solvent water serves as the proton source across all the potentials of interest.

Our systematic calculations also revealed several critical phenomena essential for accurate CO<sub>2</sub>RR modeling. First, compared to the results from ECW theory developed by Carter's group, we observed higher reaction barriers in our RPA calculations. We hypothesize that this discrepancy may arise from differences in the explicit solvent model and reactant state used, since considering hydronium ions as the proton source, as demonstrated by Bell and Head-Gordon, significantly underestimates the PCET barriers. Second, while previous theoretical studies suggested that \*CO could be hydrogenated via surface \*H at moderately negative potentials, our results indicate that although the surface reaction might be facile under such conditions, it is likely limited by the Volmer step, especially in alkaline environments, as revealed by RPA calculations. Third, the existence of \*OH on the surface, as observed in experimental spectroscopy, is challenging to model using GGA-level functional. We found that both PBE and RPBE functionals predict that \*OH would easily desorb to form OH<sup>-</sup>, while RPA predicts a much wider potential range for adsorbed \*OH stability, which has been proven to play an important role in CO<sub>2</sub>RR selectivity and surface restructuring. This finding underscores the limitations of commonly used PBE and RPBE functionals in modeling such processes. Lastly, since post-HF methods are computationally expensive, RPBE is often employed in CO<sub>2</sub>RR modeling due to its similar adsorption energy towards \*CO compared to RPA. However, when \*H<sub>2</sub>O is involved in the reaction, RPBE fails to accurately capture H<sub>2</sub>O adsorption, as it strongly underestimates its adsorption energy, whereas PBE provides a similar H<sub>2</sub>O adsorption behavior to RPA but severely overestimates CO binding

energy. This "seesaw" relationship underscores the need for caution in future CO<sub>2</sub>RR modeling efforts when using DFT-GGA functionals.

Despite the qualitative agreement of our RPA-derived mechanism with experimental observations, several limitations remain. First, as shown in Figure 6c, the reaction barriers calculated using RPA on Cu(100) surface are high, resulting in very low reaction rates. While this phenomenon aligns with the experimental results on a perfect Cu(100) surface, modeling on more representative active sites, such as steps or kinks as suggested in our recent work<sup>43</sup>, would yield more insightful information. Further research into CO<sub>2</sub>RR modeling on defective surfaces would be highly valuable but challenging with the RPA approach due to the larger unit cell size. Additionally, the transition state of the PCET process varies with electrode potential, and under reductive conditions, the surface may be covered with certain coverages of \*H or \*OH, which were not accounted for in our model. These limitations are primarily due to the extremely high computational cost of RPA when studying extended surfaces. Recent developments in embedded RPA have reduced the computational cost by approximately two orders of magnitude<sup>44</sup>, making it a promising approach for future studies on larger and more complex heterogeneous catalytic systems.

## IV. Methods

**Random phase approximation (RPA).** We calculated total energies using the Adiabatic Connection Fluctuation Dissipation Theorem (ACFDT) in its RPA, a method originating from many body perturbation theory that has been reformulated within the framework of density functional theory<sup>45-47</sup>. The total energy expression within RPA can be written as:

$$E^{RPA} = E^{EXX}([\Psi_{occ,vaccum}]) + E_c^{RPA}([\Psi_{occ,vaccum}, \Psi_{uocc,vaccum}])$$

where  $E^{RPA}$  denotes the RPA total energy. This energy is composed of  $E^{EXX}$  the exact exchange energy, which only depends on the occupied orbitals  $\Psi_{occ,vaccum}$ , and the RPA correlation energy  $E_c^{RPA}$ , which depends on all occupied and unoccupied  $\Psi_{occ,vaccum}$  and  $\Psi_{uocc,vaccum}$ . We

introduced the vacuum notation to differentiate these orbitals with the presence of implicit solvation, which will be discussed in the following section.

**RPA with Implicit Solvation.** It is important to emphasize that the correlation energy,  $E_c^{RPA}([\Psi_{occ}, \Psi_{uocc}])$ , entirely dependent on the orbitals. First, the orbitals considering solvation effects at the DFT level can be obtained using the linearized Poisson-Boltzmann equation, as implemented by Hennig et al.<sup>48</sup>. Consequently, the occupied orbitals with presence of implicit solvation,  $\Psi_{occ,solvation}$ , are derived. The unoccupied orbitals,  $\Psi_{uocc,solvation}$ , are obtained through a diagonalization step, as done in typical RPA calculations. Using these orbitals and incorporating the solvation energy, based on the electron density determined by the occupied orbitals, allows us to compute RPA energetics that include implicit solvation effects.

$$E_{sol}^{RPA} = E^{EXX}([\Psi_{occ,solvation}]) + E_c^{RPA}([\Psi_{occ,solvation}, \Psi_{uocc,solvation}]) + E^{solvation}([\Psi_{occ,solvation}])$$

where the solvation energy  $E^{solvation}([\Psi_{occ,solvation}])$  obtained in the non-self consistent HF step, and essentially this term only depends on the charge density. Nevertheless, the RPA-sol energy is not simply the vacuum RPA energy plus this solvation energy: the orbitals with the presence of implicit solvation,  $\Psi_{occ/uocc,solvation}$ , gives nontrivial contribution to the exchange and correlation components in the RPA-sol energy as well. In this work, all RPA energies are considered as RPA-sol energies unless otherwise specified.

**RPA Energetics Details.** All RPA energetics in this work were based on PBE geometries. The focus on both occupied and unoccupied orbitals in RPA calculations introduces two main challenges: First, the true orbitals are unknown and are typically approximated by those obtained from semi-local DFT functionals<sup>20, 49-50</sup>. In the case of CO adsorption, our previous research demonstrated that RPA calculations using orbitals from PBE (RPA@PBE) and RPBE (RPA@RPBE) yield nearly identical results<sup>21</sup>. Therefore, in this study, we rely on RPA calculations using the PBE-derived orbitals and one-electron energies (RPA@PBE). Second, although an infinite number of unoccupied orbitals theoretically exist, all the orbitals should be considered to accurately compute  $E_c^{RPA}$ . However, evaluating expressions for an infinite number of orbitals is

not possible in a practical computational setting. In practical implementations,  $E_{cut}^\chi$  is evaluated at different orbital cutoff energies, and is extrapolated to an infinite orbital cut-off energy using

$$E_c^{RPA}(E_{cut}^\chi) = E_c^{RPA}(\infty) + \frac{A}{E_{cut}^{\chi \frac{2}{3}}}$$

Even though  $E_c^{RPA}$  is extrapolated to infinite orbital cut-off energy, extrapolations based on higher  $E_{cut}^\chi$  values improve the accuracy. At the same time, a higher  $E_{cut}^\chi$  significantly increases the cost of calculations and in many cases makes the modeling of extended, periodic systems unfeasible. Our previous benchmark showed that at  $E_{cut}^\chi = 200 \text{ eV}$ , the convergence of absolute RPA CO adsorption energy is achieved. To model the extended system, a k-point mesh is required, but the number of k-points included in the computational modeling is directly related to the computational cost. Especially for RPA calculations with high cutoff energy, employing a dense k-point mesh can be computationally prohibitive. Therefore, we implemented the k-space ONIOM like scheme<sup>21</sup> to describe the energetics. For the  $3 \times 2$  surface models, the energy is calculated using:

$$\begin{aligned} E^{RPA}(200 \text{ eV}, 4 \times 6 \times 1) \\ &= E^{RPA}(200 \text{ eV}, 3 \times 4 \times 1) + E^{RPA}(100 \text{ eV}, 4 \times 6 \times 1) \\ &\quad - E^{RPA}(100 \text{ eV}, 3 \times 4 \times 1) \end{aligned}$$

For the detailed benchmark, see our previous work<sup>26</sup>.

**Computational setup.** All calculations in this paper were carried out using the Vienna Ab-Initio Simulation Package (VASP)<sup>51</sup>. The DFT calculations utilized a plane-wave basis set with a cutoff energy of 550 eV<sup>52</sup>. Core electrons were treated with the projector augmented wave (PAW) method. GW pseudopotentials were used for all calculations. Second order Methfessel-Paxton smearing with sigma value of 0.2 eV was used for all DFT slab optimizations and gaussian smearing with sigma value of 0.05 eV was used for molecular references.

The slab calculations were conducted in a  $3 \times 2$  unit cell of a three-layer slab. We use the experimental lattice constant of  $3.615 \text{ \AA}$ <sup>53</sup> for PBE, RPBE and RPA, which provides a balanced compromise between the PBE value of  $3.629 \text{ \AA}$  and the RPA value of  $3.581 \text{ \AA}$ . This selection

allows RPA calculations to utilize PBE-optimized structures. Repeated images of the slabs are separated by 15 Å. Dipole corrections were applied during the DFT calculations. During optimization, the bottom layer of Cu atoms was kept fixed, while the top two layers were allowed to relax. A (6×8×1) k-point mesh was used. Structural convergence was achieved when forces were below 0.01 eV/Å.

The transition states were identified using the combination of climbing image nudged elastic band (CI-NEB) method and dimmer method<sup>54</sup>. To model the explicit solvent, we employed a water cluster consisting of three water molecules. This configuration was chosen as it effectively prevents the unphysical intrusion of the implicit solvent into the solvation shell. Additionally, the three-water cluster model has been shown to accurately reproduce experimental solvation energies for hydroxide<sup>18</sup>.

The implicit solvation effects were described using the VASPsol package<sup>48</sup>, which implements linearized Poisson Boltzmann model. The dielectric constant of water, 78.4, and the Debye screening length corresponding to 1 M concentration of electrolytes, 3.0 Å were used. We chose the dielectric constant of bulk water, though the dielectric constant near a metal surface is likely much lower, because we expect that the electrolyte model we utilized combines explicit and continuum representations. Previous benchmarks have demonstrated that the dielectric constant has a minimal impact on reaction barriers<sup>18</sup>.

For all DFT methods, the energy of molecular reference energies (CO, H<sub>2</sub> and H<sub>2</sub>O) were calculated using a 15×16×17 Å<sup>3</sup> supercell to suppress the spurious interactions between periodic images. RPA calculations are based on optimized PBE structures, and the values were extrapolated to the isolated molecule limit based on a series of calculations with different box sizes (7×8×9 Å<sup>3</sup>, 8×9×10 Å<sup>3</sup>, 9×10×11 Å<sup>3</sup>, and 10×11×12 Å<sup>3</sup> for  $E_{cut}^X = 200$  eV and 250 eV, and additional 11×12×13 Å<sup>3</sup> for  $E_{cut}^X = 100$  eV and 150 eV). Molecular calculations were performed with a  $\Gamma$  point only k-point mesh. The vibrational frequencies were calculated within the harmonic approximation using the PBE functional and frequencies below 50 cm<sup>-1</sup> were reset to 50 cm<sup>-1</sup>. The calculated electronic energies were converted into free energies as follows: for surface species, only vibrational entropies were accounted for, while for gas phase molecules, both translational and rotational

entropies were included in addition to vibrational contributions. The fugacity values of gas molecules are taken from Ref<sup>14</sup>.

**Surface Charging (SC) and Extrapolated RPA-SC Energetics.** In the computational hydrogen electrode (CHE) approach<sup>55</sup>, the total chemical potential of the proton-electron pair as a function of applied potential, at all temperature and pH values, can be calculated as:

$$\mu(H^+) + \mu(e^-) = \frac{1}{2}E(H_2) - \ln(10)k_B T \cdot pH - eU_{SHE}$$

Surface charging method is within the framework of grand canonical density functional theory (GCDFT). Details can be found in our previous work<sup>28-29,56</sup>, and here we summarize the key points. The grand canonical electronic energy of a surface model,  $\Omega(U)$ , is obtained as:

$$\Omega(U) = E_{surface} - n_{surface} \mu_{electron}$$

Where the  $E_{surface}$  and  $n_{surface}$  represent the DFT energy for charged surface and the net charge of the electrons, respectively,  $\mu_{electron}$  is the chemical potential of electron, which is defined as:

$$\mu_{electron} = qU_{vac} = -eU_{vac}$$

where  $U_{vac}$  is the potential of the system with reference to the vacuum level and  $q$  is the charge of an electron. For the metallic systems, the potential-dependent grand canonical energy,  $\Omega(U)$ , exhibits a quadratic behavior around the potential of zero charge ( $U_0$ ) in the vacuum scale:

$$\Omega(U) = \Omega(U_0) - \frac{1}{2}C(U - U_0)^2$$

Where  $C$  is the capacitance of the surface. The potential of the system with respect to the standard hydrogen electrode (SHE) can be converted from  $U_{vac}$  as:  $U_{SHE} = U_{vac} - 4.44$

The fully grand canonical treatment at the RPA level, namely RPA-SC, has been developed very recently but requires extra computational cost and is not affordable for this system<sup>57</sup>. Therefore, in this work, we present the extrapolated RPA-SC energetics using RPA-N, RPBE-SC, and RPBE-N

energetics (N represents neutral condition), as the RPBE energetics are more similar to RPA ones than PBE ones:

$$\Delta\Omega_{\text{extroplated}}^{\text{RPA-SC}}(U) = \Delta\Omega^{\text{RPA-N}} + \Delta\Omega^{\text{RPBE-SC}}(U) - \Delta\Omega^{\text{RPBE-N}}$$

For all SC calculations, symmetric slabs consisting of five layers were used, created by symmetrizing the three-layer, 3×2 cell slab models. A slab separation of at least 60 Å (> 15 λ<sub>D</sub> where λ<sub>D</sub> is the Debye screening length) was used to ensure the convergence of the electrolyte density. The symmetric model ensures a well-defined vacuum energy level.

## Reference

1. Yang, Y.; Louisia, S.; Yu, S.; Jin, J.; Roh, I.; Chen, C.; Fonseca Guzman, M. V.; Feijoo, J.; Chen, P. C.; Wang, H.; Pollock, C. J.; Huang, X.; Shao, Y. T.; Wang, C.; Muller, D. A.; Abruna, H. D.; Yang, P., Operando studies reveal active Cu nanograins for CO<sub>2</sub> electroreduction. *Nature* **2023**, *614* (7947), 262-269.
2. Ross, M. B.; De Luna, P.; Li, Y. F.; Dinh, C. T.; Kim, D.; Yang, P.; Sargent, E. H., Designing materials for electrochemical carbon dioxide recycling. *Nat. Catal.* **2019**, *2* (8), 648-658.
3. Nitopi, S.; Bertheussen, E.; Scott, S. B.; Liu, X.; Engstfeld, A. K.; Horch, S.; Seger, B.; Stephens, I. E. L.; Chan, K.; Hahn, C.; Norskov, J. K.; Jaramillo, T. F.; Chorkendorff, I., Progress and Perspectives of Electrochemical CO<sub>2</sub> Reduction on Copper in Aqueous Electrolyte. *Chem. Rev.* **2019**, *119* (12), 7610-7672.
4. Cheng, D.; Zhao, Z. J.; Zhang, G.; Yang, P.; Li, L.; Gao, H.; Liu, S.; Chang, X.; Chen, S.; Wang, T.; Ozin, G. A.; Liu, Z.; Gong, J., The nature of active sites for carbon dioxide electroreduction over oxide-derived copper catalysts. *Nat. Commun.* **2021**, *12* (1), 395.
5. Zhang, G.; Zhao, Z. J.; Cheng, D.; Li, H.; Yu, J.; Wang, Q.; Gao, H.; Guo, J.; Wang, H.; Ozin, G. A.; Wang, T.; Gong, J., Efficient CO<sub>2</sub> electroreduction on facet-selective copper films with high conversion rate. *Nat. Commun.* **2021**, *12* (1), 5745.
6. Liu, X.; Schlexer, P.; Xiao, J.; Ji, Y.; Wang, L.; Sandberg, R. B.; Tang, M.; Brown, K. S.; Peng, H.; Ringe, S.; Hahn, C.; Jaramillo, T. F.; Norskov, J. K.; Chan, K., pH effects on the electrochemical reduction of CO<sub>(2)</sub> towards C<sub>(2)</sub> products on stepped copper. *Nat. Commun.* **2019**, *10* (1), 32.
7. Gunathunge, C. M.; Li, X.; Li, J.; Hicks, R. P.; Ovalle, V. J.; Waegele, M. M., Spectroscopic Observation of Reversible Surface Reconstruction of Copper Electrodes under CO<sub>2</sub> Reduction. *J. Phys. Chem. C* **2017**, *121* (22), 12337-12344.
8. Liu, X.; Xiao, J.; Peng, H.; Hong, X.; Chan, K.; Norskov, J. K., Understanding trends in electrochemical carbon dioxide reduction rates. *Nat. Commun.* **2017**, *8*, 15438.
9. Peng, H.; Tang, M. T.; Liu, X.; Schlexer Lamoureux, P.; Bajdich, M.; Abild-Pedersen, F., The role of atomic carbon in directing electrochemical CO<sub>(2)</sub> reduction to multicarbon products. *Energy Environ. Sci.* **2021**, *14* (1), 473-482.

10. Goodpaster, J. D.; Bell, A. T.; Head-Gordon, M., Identification of Possible Pathways for C-C Bond Formation during Electrochemical Reduction of CO<sub>2</sub>: New Theoretical Insights from an Improved Electrochemical Model. *J. Phys. Chem. Lett.* **2016**, *7* (8), 1471-7.
11. Li, J.; Chang, X.; Zhang, H.; Malkani, A. S.; Cheng, M. J.; Xu, B.; Lu, Q., Electrokinetic and in situ spectroscopic investigations of CO electrochemical reduction on copper. *Nat. Commun.* **2021**, *12* (1), 3264.
12. Chang, X.; Li, J.; Xiong, H.; Zhang, H.; Xu, Y.; Xiao, H.; Lu, Q.; Xu, B., C-C Coupling Is Unlikely to Be the Rate-Determining Step in the Formation of C(2+) Products in the Copper-Catalyzed Electrochemical Reduction of CO. *Angew. Chem. Int. Ed.* **2022**, *61* (2), e202111167.
13. Shao, F.; Xia, Z.; You, F.; Wong, J. K.; Low, Q. H.; Xiao, H.; Yeo, B. S., Surface Water as an Initial Proton Source for the Electrochemical CO Reduction Reaction on Copper Surfaces. *Angew. Chem. Int. Ed.* **2023**, *62* (3), e202214210.
14. Peterson, A. A.; Abild-Pedersen, F.; Studt, F.; Rossmeisl, J.; Nørskov, J. K., How copper catalyzes the electroreduction of carbon dioxide into hydrocarbon fuels. *Energy Environ. Sci.* **2010**, *3* (9), 1311.
15. Nie, X.; Esopi, M. R.; Janik, M. J.; Asthagiri, A., Selectivity of CO<sub>(2)</sub> reduction on copper electrodes: the role of the kinetics of elementary steps. *Angew. Chem. Int. Ed.* **2013**, *52* (9), 2459-62.
16. Cheng, T.; Xiao, H.; Goddard, W. A., 3rd, Full atomistic reaction mechanism with kinetics for CO reduction on Cu(100) from ab initio molecular dynamics free-energy calculations at 298 K. *Proc. Natl. Acad. Sci. USA* **2017**, *114* (8), 1795-1800.
17. Xiao, H.; Cheng, T.; Goddard, W. A., 3rd, Atomistic Mechanisms Underlying Selectivities in C(1) and C(2) Products from Electrochemical Reduction of CO on Cu(111). *J. Am. Chem. Soc.* **2017**, *139* (1), 130-136.
18. Gauthier, J. A.; Lin, Z.; Head-Gordon, M.; Bell, A. T., Pathways for the Formation of C<sub>2+</sub> Products under Alkaline Conditions during the Electrochemical Reduction of CO<sub>2</sub>. *ACS Energy Lett.* **2022**, *7* (5), 1679-1686.
19. Schimka, L.; Harl, J.; Stroppa, A.; Gruneis, A.; Marsman, M.; Mittendorfer, F.; Kresse, G., Accurate surface and adsorption energies from many-body perturbation theory. *Nat. Mater.* **2010**, *9* (9), 741-4.
20. Ren, X.; Rinke, P.; Scheffler, M., Exploring the random phase approximation: Application to CO adsorbed on Cu(111). *Phys. Rev. B* **2009**, *80* (4).
21. Wei, Z.; Goltl, F.; Sautet, P., Diffusion Barriers for Carbon Monoxide on the Cu(001) Surface Using Many-Body Perturbation Theory and Various Density Functionals. *J. Chem. Theory Comput.* **2021**, *17* (12), 7862-7872.
22. Zhao, Q.; Martirez, J. M. P.; Carter, E. A., Revisiting Understanding of Electrochemical CO<sub>2</sub> Reduction on Cu(111): Competing Proton-Coupled Electron Transfer Reaction Mechanisms Revealed by Embedded Correlated Wavefunction Theory. *J. Am. Chem. Soc.* **2021**, *143* (16), 6152-6164.
23. Zhao, Q.; Carter, E. A., Revisiting Competing Paths in Electrochemical CO<sub>2</sub> Reduction on Copper via Embedded Correlated Wavefunction Theory. *J. Chem. Theory Comput.* **2020**, *16* (10), 6528-6538.
24. Schmidt, P. S.; Thygesen, K. S., Benchmark Database of Transition Metal Surface and Adsorption Energies from Many-Body Perturbation Theory. *J. Phys. Chem. C* **2018**, *122* (8), 4381-4390.

25. Hellgren, M.; Baguet, L., Random phase approximation with exchange for an accurate description of crystalline polymorphism. *Phys. Rev. Res.* **2021**, *3* (3).
26. Wei, Z.; Sautet, P., Improving the Accuracy of Modelling CO<sub>2</sub> Electroreduction on Copper Using Many-Body Perturbation Theory. *Angew. Chem. Int. Ed.* **2022**, *61* (43), e202210060.
27. Zhang, Z.; Gee, W.; Sautet, P.; Alexandrova, A. N., H and CO Co-Induced Roughening of Cu Surface in CO<sub>2</sub> Electroreduction Conditions. *J. Am. Chem. Soc.* **2024**, *146* (23), 16119-16127.
28. Cheng, D.; Wei, Z.; Zhang, Z.; Broekmann, P.; Alexandrova, A. N.; Sautet, P., Restructuring and Activation of Cu(111) under Electrocatalytic Reduction Conditions. *Angew. Chem. Int. Ed.* **2023**, *62* (20), e202218575.
29. Cheng, D.; Alexandrova, A. N.; Sautet, P., H-Induced Restructuring on Cu(111) Triggers CO Electroreduction in an Acidic Electrolyte. *J. Phys. Chem. Lett.* **2024**, 1056-1061.
30. Li, C. Y.; Le, J. B.; Wang, Y. H.; Chen, S.; Yang, Z. L.; Li, J. F.; Cheng, J.; Tian, Z. Q., In situ probing electrified interfacial water structures at atomically flat surfaces. *Nat. Mater.* **2019**, *18* (7), 697-701.
31. Le, J. B.; Fan, Q. Y.; Li, J. Q.; Cheng, J., Molecular origin of negative component of Helmholtz capacitance at electrified Pt(111)/water interface. *Sci. Adv.* **2020**, *6* (41).
32. Vavra, J.; Ramona, G. P. L.; Dattila, F.; Kormányos, A.; Priamushko, T.; Albertini, P. P.; Loiudice, A.; Cherevko, S.; Lopéz, N.; Buonsanti, R., Solution-based Cu<sup>+</sup> transient species mediate the reconstruction of copper electrocatalysts for CO<sub>2</sub> reduction. *Nat. Catal.* **2024**, *7* (1), 89-97.
33. Sun, M.; Staykov, A.; Yamauchi, M., Understanding the Roles of Hydroxide in CO<sub>2</sub> Electroreduction on a Cu Electrode for Achieving Variable Selectivity. *ACS Catal.* **2022**, *12* (24), 14856-14863.
34. Herzog, A.; Lopez Luna, M.; Jeon, H. S.; Rettenmaier, C.; Grosse, P.; Bergmann, A.; Roldan Cuenya, B., Operando Raman spectroscopy uncovers hydroxide and CO species enhance ethanol selectivity during pulsed CO<sub>2</sub> electroreduction. *Nat. Commun.* **2024**, *15* (1), 3986.
35. Okura, Y.; Santis, G. D.; Hirata, K.; Melissas, V. S.; Ishiuchi, S. I.; Fujii, M.; Xantheas, S. S., Switching of Protonation Sites in Hydrated Nicotine via a Grotthuss Mechanism. *J. Am. Chem. Soc.* **2024**, *146* (5), 3023-3030.
36. Farnesi Camellone, M.; Negreiros Ribeiro, F.; Szabova, L.; Tateyama, Y.; Fabris, S., Catalytic Proton Dynamics at the Water/Solid Interface of Ceria-Supported Pt Clusters. *J. Am. Chem. Soc.* **2016**, *138* (36), 11560-7.
37. Li, G.; Wang, B.; Resasco, D. E., Water-Mediated Heterogeneously Catalyzed Reactions. *ACS Catal.* **2019**, *10* (2), 1294-1309.
38. Reocreux, R.; Girel, E.; Clabaut, P.; Tuel, A.; Besson, M.; Chaumonnot, A.; Cabiac, A.; Sautet, P.; Michel, C., Reactivity of shape-controlled crystals and metadynamics simulations locate the weak spots of alumina in water. *Nat. Commun.* **2019**, *10* (1), 3139.
39. Lamoureux, P. S.; Singh, A. R.; Chan, K., pH Effects on Hydrogen Evolution and Oxidation over Pt(111): Insights from First-Principles. *ACS Catal.* **2019**, *9* (7), 6194-6201.
40. Chen, L. D.; Bajdich, M.; Martirez, J. M. P.; Krauter, C. M.; Gauthier, J. A.; Carter, E. A.; Luntz, A. C.; Chan, K.; Norskov, J. K., Understanding the apparent fractional charge of protons in the aqueous electrochemical double layer. *Nat. Commun.* **2018**, *9* (1), 3202.
41. Wang, L.; Nitopi, S. A.; Bertheussen, E.; Orazov, M.; Morales-Guio, C. G.; Liu, X.; Higgins, D. C.; Chan, K.; Nørskov, J. K.; Hahn, C.; Jaramillo, T. F., Electrochemical Carbon Monoxide Reduction on Polycrystalline Copper: Effects of Potential, Pressure, and pH on Selectivity toward Multicarbon and Oxygenated Products. *ACS Catal.* **2018**, *8* (8), 7445-7454.

42. Scholten, F.; Nguyen, K. C.; Bruce, J. P.; Heyde, M.; Roldan Cuenya, B., Identifying Structure-Selectivity Correlations in the Electrochemical Reduction of CO<sub>2</sub> : A Comparison of Well-Ordered Atomically Clean and Chemically Etched Copper Single-Crystal Surfaces. *Angew. Chem. Int. Ed.* **2021**, *60* (35), 19169-19175.
43. Cheng, D.; Nguyen, K.-L. C.; Sumaria, V.; Wei, Z.; Zhang, Z.; Gee, W.; Li, Y.; Morales-Guio, C. G.; Heyde, M.; Roldan Cuenya, B.; Alexandrova, A. N.; Sautet, P., Structure Sensitivity and Catalyst Restructuring for CO<sub>2</sub> Electro-reduction on Copper. *ChemRxiv* **2024**, doi: 10.26434/chemrxiv-2024-z3dlp-v2.
44. Wei, Z.; Martirez, J. M. P.; Carter, E. A., Introducing the embedded random phase approximation: H<sub>2</sub> dissociative adsorption on Cu(111) as an exemplar. *J. Chem. Phys.* **2023**, *159* (19).
45. Niquet, Y. M.; Fuchs, M.; Gonze, X., Exchange-correlation potentials in the adiabatic connection fluctuation-dissipation framework. *Phys. Rev. A* **2003**, *68* (3).
46. Langreth, D. C.; Perdew, J. P., Exchange-correlation energy of a metallic surface: Wave-vector analysis. *Phys. Rev. B* **1977**, *15* (6), 2884-2901.
47. Dahlen, N. E.; van Leeuwen, R.; von Barth, U., Variational energy functionals of the Green function and of the density tested on molecules. *Phys. Rev. A* **2006**, *73* (1).
48. Mathew, K.; Sundararaman, R.; Letchworth-Weaver, K.; Arias, T. A.; Hennig, R. G., Implicit solvation model for density-functional study of nanocrystal surfaces and reaction pathways. *J. Chem. Phys.* **2014**, *140* (8), 084106.
49. Furche, F., Developing the random phase approximation into a practical post-Kohn-Sham correlation model. *J. Chem. Phys.* **2008**, *129* (11), 114105.
50. Fuchs, M.; Gonze, X., Accurate density functionals: Approaches using the adiabatic-connection fluctuation-dissipation theorem. *Phys. Rev. B* **2002**, *65* (23).
51. Kresse, G.; Furthmüller, J., Efficiency of ab-initio total energy calculations for metals and semiconductors using a plane-wave basis set. *Comput. Mater. Sci.* **1996**, *6* (1), 15-50.
52. Kresse, G.; Furthmüller, J., Efficient iterative schemes for ab initio total-energy calculations using a plane-wave basis set. *Phys. Rev. B Condens Matter* **1996**, *54* (16), 11169-11186.
53. Janthon, P.; Luo, S. A.; Kozlov, S. M.; Vines, F.; Limtrakul, J.; Truhlar, D. G.; Illas, F., Bulk Properties of Transition Metals: A Challenge for the Design of Universal Density Functionals. *J. Chem. Theory Comput.* **2014**, *10* (9), 3832-9.
54. Henkelman, G.; Uberuaga, B. P.; Jónsson, H., A climbing image nudged elastic band method for finding saddle points and minimum energy paths. *J. Chem. Phys.* **2000**, *113* (22), 9901-9904.
55. Norskov, J. K.; Rossmeisl, J.; Logadottir, A.; Lindqvist, L.; Kitchin, J. R.; Bligaard, T.; Jónsson, H., Origin of the overpotential for oxygen reduction at a fuel-cell cathode. *J. Phys. Chem. B* **2004**, *108* (46), 17886-17892.
56. Steinmann, S. N.; Sautet, P., Assessing a First-Principles Model of an Electrochemical Interface by Comparison with Experiment. *J. Phys. Chem. C* **2016**, *120* (10), 5619-5623.
57. Wei, Z.; Goltl, F.; Steinmann, S. N.; Sautet, P., Modeling Electrochemical Processes with Grand Canonical Treatment of Many-Body Perturbation Theory. *J. Phys. Chem. Lett.* **2022**, *13* (26), 6079-6084.

## **Acknowledgments**

The work was supported by the National Science Foundation CBET grant 2103116 and the Audi CO<sub>2</sub> Cy Pres Award. Computational resources for this work were provided by the UCLA-shared cluster Hoffman2, and the Expanse cluster through the allocation CHE170060 at the San Diego Supercomputing Center through ACCESS.

## **Data Availability**

The data that support the findings of this study are available from the corresponding author upon reasonable request.

## **Conflict of Interest**

The authors declare no conflict of interest.